Probing autoionizing states of molecular oxygen with XUV transient absorption: Electronic-symmetry-dependent line shapes and laser-induced modifications

Chen-Ting Liao,[1] Xuan Li,[2] Daniel J. Haxton,[2] Thomas N. Rescigno,[2] Robert R. Lucchese,[3] C. William McCurdy,[2,4,*] and Arvinder Sandhu[1,†]

[1]*College of Optical Sciences and Department of Physics, University of Arizona, Tucson, Arizona 85721, USA*
[2]*Chemical Sciences Division, Lawrence Berkeley National Laboratory, Berkeley, California 94720, USA*
[3]*Chemistry Department, Texas A&M University, College Station, Texas 77842, USA*
[4]*Department of Chemistry, University of California, Davis, California 95616, USA*

(Received 16 November 2016; published 26 April 2017)

We used extreme ultraviolet (XUV) transient absorption spectroscopy to study the autoionizing Rydberg states of oxygen in an electronically- and vibrationally-resolved fashion. XUV pulse initiates molecular polarization and near-infrared pulse perturbs its evolution. Transient absorption spectra show positive optical-density (OD) change in the case of $ns\sigma_g$ and $nd\pi_g$ autoionizing states of oxygen and negative OD change for $nd\sigma_g$ states. Multiconfiguration time-dependent Hartree-Fock (MCTDHF) calculations are used to simulate the transient absorption and the resulting spectra and temporal evolution agree with experimental observations. We model the effect of near-infrared perturbation on molecular polarization and find that the laser-induced phase-shift model agrees with the experimental and MCTDHF results, while the laser-induced attenuation model does not. We relate the electronic-state-symmetry-dependent sign of the OD change to the Fano parameters of the static absorption line shapes.

DOI: 10.1103/PhysRevA.95.043427

I. INTRODUCTION

The interaction of extreme ultraviolet (XUV) radiation with small molecules results in the formation of highly excited molecular states that evolve on ultrafast time scales and govern the dynamics of many physical and chemical phenomena observed in nature [1,2]. In particular, single excitations of valence or inner valence electrons to Rydberg molecular orbitals form neutral states that lie above the ionization threshold (sometimes called "superexcited" states) [3]. These states can lie energetically above several of the excited states of the molecular ion into which they can decay through autoionization [4]. Another feature of these autoionizing states is strong state-mixing and coupled electronic and nuclear motions, which can result in fast dissociation into excited neutral fragments [5]. The motivation for investigation of these states is quite wide ranging, from better understanding of the solar radiation induced photochemistry of planetary atmospheres [6] to the ultraviolet radiation damage in biological systems [7]. Furthermore, these are the states whose dynamics provide a mechanism for dissociative recombination of electrons with molecular ions, which has been the subject of decades of research [8–13]. Due to their importance in complex processes, the direct observation of the electronic and nuclear dynamics of these states has been a topic of intense interest in molecular physics.

Advances in ultrafast technology such as laser high-harmonic generation (HHG) have enabled femtosecond (10^{-15} s) and attosecond (10^{-18} s) light pulses in the energy range of 10–100's eV [14,15]. These ultrashort and broadband XUV bursts provide a way to coherently prepare, probe, and control ultrafast dynamics of highly excited molecules [16,17]. Combined with time-delayed near-infrared (NIR) or visible laser pulses, pump-probe spectroscopy schemes can be used to investigate dynamics in atoms and molecules on the natural time scale of electrons [18].

To characterize excited-state dynamics, researchers have developed sophisticated techniques involving the detection of charged photofragments, and the measurement of the photoabsorption signals. In particular, attosecond transient absorption spectroscopy (ATAS) has received considerable attention recently [19,20], as it is relatively easy to implement and quite suitable for the measurement and manipulation of bound- and quasibound-state dynamics. Recent ATAS experiments focused on properties and evolution of XUV initiated dipole polarization in atoms by using a delayed NIR pulse as a perturbation. In this scenario, many interesting time-dependent phenomena have been observed, including ac Stark shifts [21], light-induced states [22], quantum beats or quantum path interferences [23], strong-field line shape control [24], and resonant-pulse-propagation induced XUV pulse reshaping effects [25,26].

In contrast to the bulk of previous studies, which have been conducted in atoms, our goal in this paper is to extend ATAS to the investigation of complex molecular systems. Molecular ATAS is a largely unexplored topic and very few studies have been conducted so far [27,28]. Here we present a joint experimental-theoretical study of the autoionizing Rydberg states of O_2. An XUV attosecond pulse train was used to coherently prepare the molecular polarization, and a time-delayed NIR pulse was used to perturb its evolution. Superexcited states created by the XUV pulse have multiple competing decay channels, including autoionization and dissociation into charged or neutral fragments. The autoionization process is one of the most fundamental processes driven by electron correlation, which involves interference between the bound and continuum channels. This discrete-continuum interaction is ubiquitous in atoms, molecules, and nanomaterials [29], and it is parametrized by the well-known Fano formula describing spectral line shapes [30].

*cwmccurdy@lbl.gov
†sandhu@physics.arizona.edu

The paper is organized as follows. Section II below introduces the autoionizing Rydberg states of O_2 and compares the photoabsorption cross sections obtained by different methods, including our time-independent Schwinger variational calculations. In Sec. III, we describe our experimental setup and transient absorption line shapes obtained at various time delays. Section IV is focused on the theoretical approach, where we describe our time-independent Schwinger calculation method in Sec. IV A, and the *ab initio* multiconfiguration time-dependent Hartree-Fock (MCTDHF) method in Sec. IV B. We then compare full experimental transient absorption spectrograms with MCTDHF calculations in Sec. IV C. In Sec. V, we present a simple model that connects Fano q parameters of static absorption profiles with the transient absorption line change shapes and we compare how laser-induced attenuation (LIA) and laser-induced phase (LIP) modify the dipole polarization initiated by the XUV pulse. We summarize our work in Sec. VI, followed by Appendixes that describe experimental details, the MCTDHF approach, and a few-level model of dipole polarization and NIR perturbation.

II. AUTOIONIZING RYDBERG STATES IN O_2

In our experiment, autoionizing Rydberg states with electronic configurations that we can denote as $2\sigma_u^{-1}(c\,^4\Sigma_u^-)nl\sigma_g$, for example, are formed through the direct XUV excitation of an inner-shell $2\sigma_u$ electron to the Rydberg series converging to the excited ionic c state ($c\,^4\Sigma_u^-$) of $O_2{}^+$. Figure 1(a) shows the potential-energy curves of some of these states. Those states that are optically connected to the $^3\Sigma_g^-$ ground state of O_2 have the symmetries $^3\Sigma_u^-$ and $^3\Pi_u$. In our observations, those Rydberg series correspond to excitations from the $2\sigma_u$ orbital of O_2 to $nd\sigma_g$ ($^3\Sigma_u^-$), $ns\sigma_g$ ($^3\Sigma_u^-$), and $nd\pi_g$ ($^3\Pi_u$). The XUV pulse in the experiment can also cause direct excitation to the $^3\Sigma_u^-$ and $^3\Pi_u$ continua by photoionization of the $3\sigma_g$, $1\pi_u$, and $1\pi_g$ valence shells. Those excitations form the $X\,^2\Pi_g$, $a\,^4\Pi_u$, $A\,^2\Pi_u$ $b\,^4\Sigma_g^-$, and $B\,^2\Sigma_g^-$ states of the ion, lying below the c state of $O_2{}^+$ [33], and also a second $^2\Pi_u$ state at 23.9 eV just below the ground vibrational level of the c state at 24.564 eV [34].

Therefore, the autoionizing Rydberg states converging to the c state are each embedded in several ionization continua, and can decay into any of them. These autoionizing Rydberg states can be grouped into pairs of dominant features $[nd\sigma_g,(n+1)s\sigma_g]$ shown in Fig. 1(a) as blue and red curves, respectively. As we discuss later the $(n+1)s\sigma_g$ series overlaps with the $nd\pi_g$ series; therefore, to be accurate, the pairs of features in Fig. 1(a) should be listed as $[nd\sigma_g, (n+1)s\sigma_g + nd\pi_g]$. The pairs relevant to our study are $[3d\sigma_g, 4s\sigma_g + 3d\pi_g]$, $[4d\sigma_g, 5s\sigma_g + 4d\pi_g]$, $[5d\sigma_g, 6s\sigma_g + 5d\pi_g]$, $[6d\sigma_g, 7s\sigma_g + 6d\pi_g]$, etc.

Furthermore, the ionic c state supports two vibrational levels [35], $v = 0$ and $v = 1$, as shown in Fig. 1(a), and the $nl\sigma_g$ Rydberg states are also known to support at least two vibrational levels.

The pairs of Rydberg features $[nd\sigma_g,(n+1)s\sigma_g + nd\pi_g]$ can be identified in the static XUV photoabsorption spectra in Fig. 1(b), where the purple curve is static absorption spectrum adapted from a synchrotron study by Holland *et al.* [31]. The autoionizing Rydberg series with vibrational state $v = 0$ are labeled at the bottom of Fig. 1(b) (blue and red labels for each pair), while the members of the series with vibrational state $v = 1$ are labeled at the top. The green curve in Fig. 1(b) shows the theoretical cross section computed by Demekhin *et al.* [32] using a single center expansion method that includes static and nonlocal exchange interactions without coupling between ionization channels leading to different ion states. These authors estimated the $v = 1$ contributions and broadened their theoretical cross sections by a Gaussian function of 20 meV full width at half maximum (FWHM).

Using the Schwinger variational method in calculations described in Sec. IV A, we computed the XUV photoionization

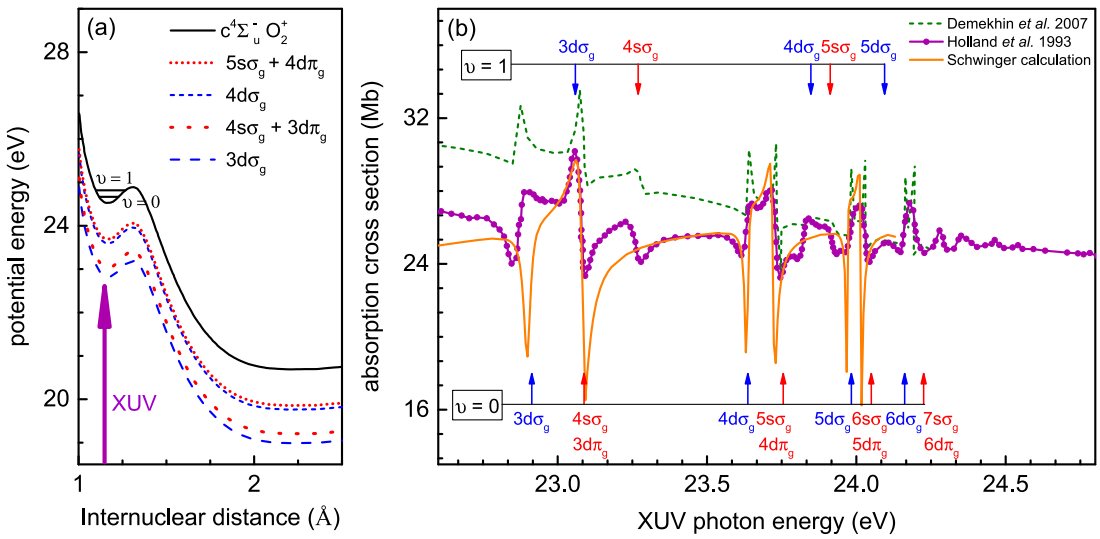

FIG. 1. (a) Schematic potential-energy diagram of O_2. Black curve is the excited ionic c state ($c\,^4\Sigma_u^-$). Blue dashed and red dotted curves are Rydberg series of neutral superexcited nd and ns states, respectively. Each state supports two vibrational levels. (b) (Purple line) Synchrotron measurement of photoabsorption cross section from [31]. Features associated with various electronic states and their vibrational levels ($v = 0$ at bottom and $v = 1$ at top) are labeled. (Green dash line) Theoretical photoabsorption cross section from [32]. (Orange solid curve) Multichannel photoabsorption cross section that we obtained using Schwinger variational calculation.

TABLE I. State assignment, effective quantum number n^*, energy, linewidth, and field-free lifetime of some relevant autoionizing states in O_2 from [31,32]. Fano q parameters are obtained by fitting the calculated photoabsorption cross section in Fig. 1(b).

State	n^*	Energy (eV)	Linewidth (meV)	Lifetime (fs)	Fano q
$6s\sigma_g$	~5	24.028	3.69	178.37	−0.60
$5d\sigma_g$		23.976	3.60	182.83	0.28
$5s\sigma_g$	~4	23.733	7.31	90.04	−0.59
$4d\sigma_g$		23.632	7.10	92.70	0.22

cross section at the equilibrium internuclear distance of O_2 to approximate the vibrational ground-state $v = 0$ contribution. Our results in Fig. 1(b) (orange curve) reproduce the main features of synchrotron measurements very well. Our calculated cross-section curve is for randomly oriented molecules and includes both perpendicular ($^3\Pi_u$) and parallel ($^3\Sigma_u^-$) contributions from various ionization channels corresponding to continua associated with different ionic states. From the calculated static absorption line shapes (orange curve), we extracted Fano q parameters for a few representative states, which are listed in Table I. The autoionization lifetimes for these states (based on Ref. [32]) are also listed in Table I.

III. TRANSIENT ABSORPTION EXPERIMENT

To explore the dynamics of O_2 superexcited states, we conducted experimental and theoretical ATAS studies. Our experimental pump-probe setup is shown in Fig. 2(a). Briefly, we employ 40 fs NIR pulses at 1 kHz repetition rate with pulse energy 2 mJ and central wavelength 780 nm. One portion of the NIR beam is focused into a xenon filled hollow-core waveguide to generate XUV attosecond pulse trains (APTs) with ~440 attosecond bursts and ~4 fs envelope. The APTs is dominated by harmonics 13, 15, and 17, out of which the 15th harmonic resonantly populates superexcited states. The second portion of NIR laser pulse goes through a delay line and perturbs the XUV initiated molecular polarization with estimated peak intensity ~1 TW/cm^2. A grating spectrometer is used to measured the XUV spectra transmitted through the O_2 gas sample. Using the Beer-Lambert law we can determine optical density change (OD) due to NIR perturbation as a function of photon energy, $\hbar\omega$, and XUV-NIR time delay, t_d, as

$$\mathrm{OD}(\omega,t_d) = -\log_{10}\left[\left(I_{\mathrm{out}}^{\mathrm{XUV+NIR}}\right)/\left(I_{\mathrm{out}}^{\mathrm{XUV}}\right)\right]. \quad (1)$$

$I_{\mathrm{out}}^{\mathrm{XUV+NIR}}(\omega,t_d)$ and $I_{\mathrm{out}}^{\mathrm{XUV}}(\omega,t_d)$ are transmitted XUV spectra with and without the presence of NIR pulse, respectively. Further details of the experimental setup are given in Appendix A.

The spectrogram measured using ATAS is shown in Fig. 2(b). To highlight the NIR induced absorbance change relative to continuum absorption, Fourier high pass filter is used to remove slow variation of underlying spectral profile, as also used in [27,36]. The vertical axis of the spectrogram refers to millioptical density change (mOD). Negative time delay means XUV arrives at the oxygen sample first, i.e., the NIR perturbation is imposed after the XUV initiates molecular polarization. There are many interesting aspects of this spectrogram, the striking feature being that we observe alternating blue and red bands corresponding to negative and positive OD change relative to the O_2^+ continua absorption spectrum, respectively. According to the assignments of the autoionizing Rydberg states in Fig. 1(b), we find that all $nd\sigma_g$ states show negative OD (less absorption compared to the continuum), while the features corresponding to the combination of $ns\sigma_g$ and $nd\pi_g$ show positive OD.

We have plotted transient absorption spectra at some representative time delays in Fig. 3(a). The experimental input XUV spectrum is also plotted. Relevant state assignments are labeled on the top of the figure. In addition to $v = 0$ states, we also list $v = 1$ states, following assignments in Ref. [32]. In Fig. 3(a), for positive time delays, when the NIR pulse arrives earlier, there are no discernible features in the transient absorption spectrum, because the NIR pulse alone is not strong enough to significantly perturb the ground state of neutral O_2. At large negative delays where the XUV arrives earlier than the NIR, we observe finer oscillating structures corresponding to the well-known perturbed free induction decay [37]. When the delay is close to zero, complicated line shapes can be observed. These line shapes are more complex than Fano profiles observed in ATAS of atomic gases. Considering different pairs of features in the series, i.e., $[4d\sigma_g, 5s\sigma_g + 4d\pi_g]$, $[5d\sigma_g, 6s\sigma_g + 5d\pi_g]$, etc., we find that all $nd\sigma_g$ features show a dip in the transient absorption line shape at the position of the resonance, while $(n+1)s\sigma_g + nd\pi_g$ show a peak. The difference in signs of OD for these features stems from the difference in Fano q parameters of the static absorption profiles

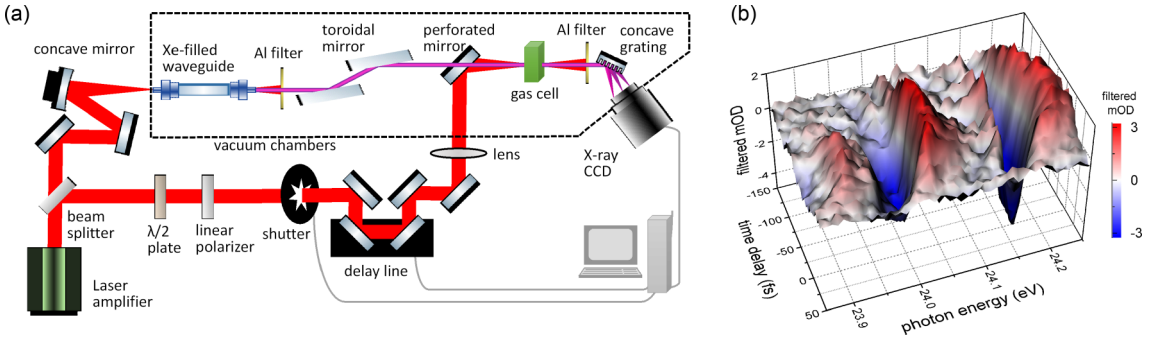

FIG. 2. (a) Experimental setup for XUV transient absorption studies in neutral superexcited states of O_2. (b) Experimentally measured transient absorption spectrogram in O_2.

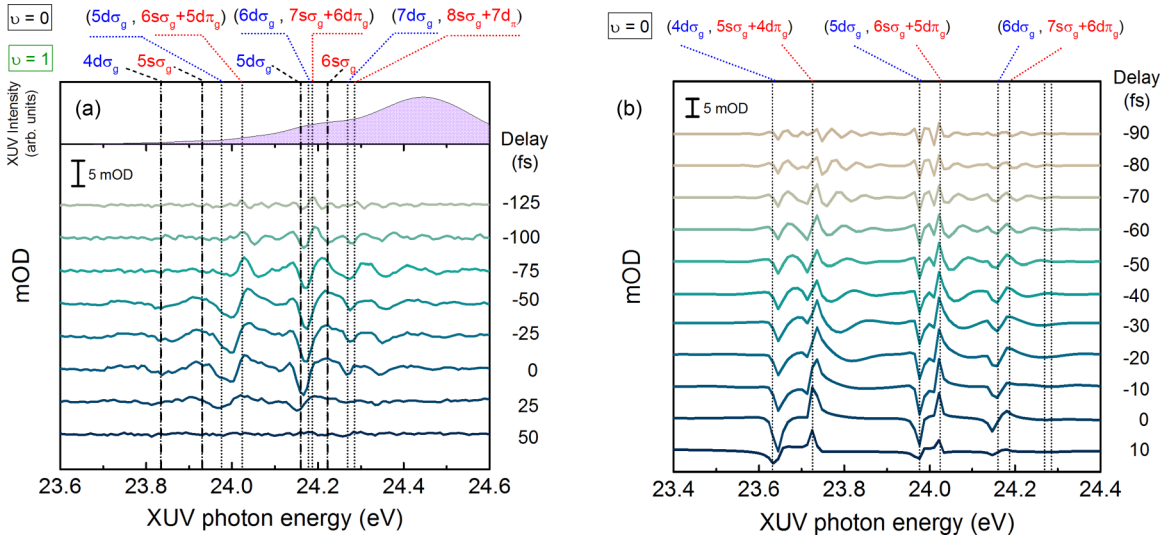

FIG. 3. (a) Experimental transient absorption spectra at certain representative time delays. The scale bar represents 5 mOD change. Experimental XUV spectrum is also shown at the top. Negative time delay implies XUV arrives at the target earlier than NIR pulse. All $nd\sigma_g$ ($ns\sigma_g$+$nd\pi_g$) states show negative (positive) OD at resonance, corresponding to less (more) absorption compared to continua absorption spectrum. (b) The MCTDHF calculations of the transient absorption spectra at few time delays.

of the corresponding states which are shown in Fig. 1(b) and discussed in more detail below.

IV. TRANSIENT ABSORPTION THEORY

A. Time-independent calculations

Since the static XUV photoabsorption line shapes play a central role in our interpretation of the transient absorption spectra, we calculated the XUV photoionization cross section using the Schwinger variational approach [38–40]. Briefly, the one-electron molecular orbitals in these calculations were expanded by using an augmented correlation-consistent polarized valence triple ζ aug-cc-pVTZ basis set [41,42]. A valence complete active space self-consistent-field calculation on the ground state of O_2 was used to obtain a set of orbitals that was then used in complete active space configuration-interaction (CAS-CI) calculations on both the O_2 ground state and the O_2^+ states. The six channels that were included consisted of five channels which are open in the energy range of interest in this study, 23.6 eV to 24.4 eV, $X\,^2\Pi_g$, $a\,^4\Pi_u$, $A\,^2\Pi_u$, $b\,^4\Sigma_g^-$, and $B\,^2\Sigma_g^-$. The sixth channel, which was closed, is the $c\,^4\Sigma_u^-$ channel that is responsible for the autoionization resonances studied here. In all calculations, the ionization potentials were shifted slightly to agree with the experimental vertical ionization potentials in Ref. [34].

In Fig. 4(a), we plot the total cross section as a function of photon energy and as a function of the effective quantum number, defined as $n^* = \sqrt{R_y/(\mathrm{IP} - \hbar\omega)}$, where R_y is the Rydberg constant and IP is the ionization potential of the closed $c\,^4\Sigma_u^-$ channel which has the autoionizing resonances. The partial cross sections computed for ionization leading to the five open channels are shown in Fig. 4(b), which shows the autoionization resonances coming from the closed channel. We neglected two states that are observed in the photoelectron spectrum [34]: the dissociative $^2\Pi_u$ state at 23.9 eV that has a broad photoelectron spectra and the weak $^2\Sigma_u^-$ channel at 27.3 eV. In addition, we have neglected a number of other experimentally unobserved states that would have very weak ionization cross sections in this energy region.

Figure 4(b) shows that Fano q parameters depend on the final channel considered. However, a single resonance interacting with many continua can be rewritten as a resonance interacting with the linear combination of the channels. The orthogonal linear combinations of the channels do not interact with the resonance but contribute to a nonzero background to the cross section. Furthermore, by calculating the parallel ($^3\Sigma_u^-$) and perpendicular ($^3\Pi_u$) polarization contributions to the XUV photoionization cross section in Fig. 4(c), we clearly see that each of the pairs of features in Fig. 1 corresponds to three states that were mentioned in Sec. II. In each pair, the first feature corresponds to an $nd\sigma_g$ Rydberg state, while the second corresponds to contributions from the $(n+1)s\sigma_g$ and $nd\pi_g$ states. The $nd\pi_g$ Rydberg series was proposed before by Wu *et al.* [43], but it has been ignored in many of the subsequent experimental and theoretical studies. Importantly, as seen from Fig. 4(c), Fano q parameters are similar for the two overlapping states $(n+1)s\sigma_g$ and $nd\pi_g$.

B. Time-dependent calculations

We performed *ab initio* theoretical calculation of transient absorption signals in the same energy range as O_2 superexcited states using a recently developed implementation of the MCTDHF method. This method simultaneously describes stable valence states, core-hole states, and the photoionization continua, which are involved in these transient absorption spectra, and this approach has been previously explored and developed by several groups [44–50]. Briefly, our implementation solves the time-dependent Schrödinger equation in full dimensionality, with all electrons active. It rigorously treats the ionization continua for both single and multiple ionization using complex exterior scaling. As more orbitals are included, the MCTDHF wave function formally converges to the exact many-electron

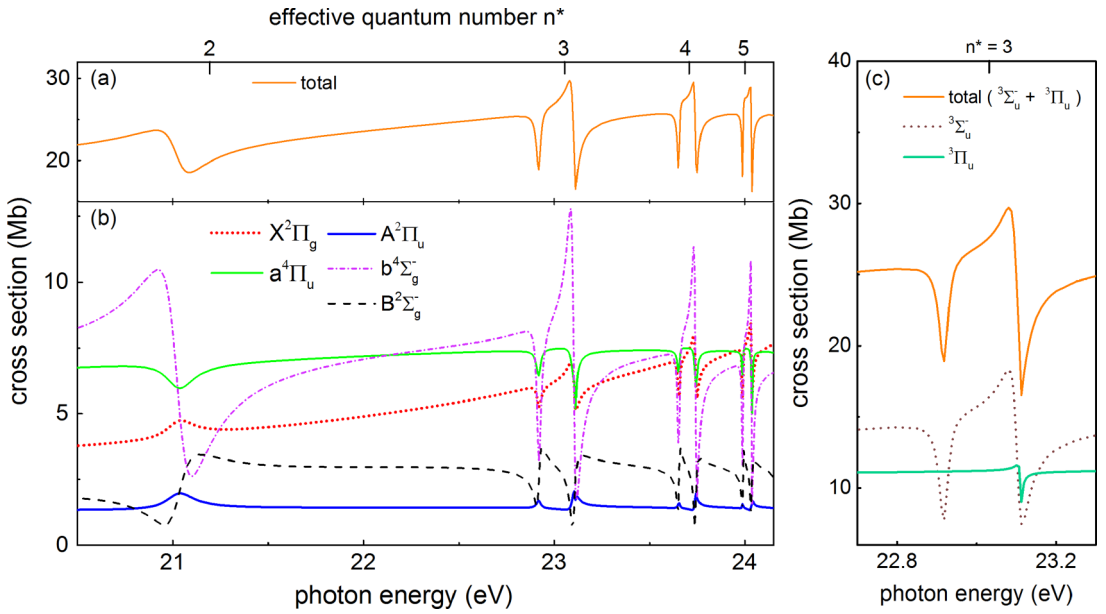

FIG. 4. (a) Total cross section as a function of the photon energy and effective quantum number n^*. (b) Various electronic channels contributing the total cross sections and their Fano profiles. (c) Parallel ($^3\Sigma_u^-$) and perpendicular ($^3\Pi_u$) polarization contributions to the total XUV photoionization cross section in the vicinity of the pair of features with $n^* = 3$ in Fig. 1 showing the presence of the $3d\sigma_g$(parallel), $4s\sigma_g$ (parallel), and $3d\pi_g$ (perpendicular) states.

solution, but here the limits of computational practicality were reached with the inclusion of full configuration interaction with nine time-dependent orbitals.

In these calculations, an isolated XUV attosecond pulse is used to excite the polarization which is then perturbed by a more intense NIR pulse. The weaker XUV probe pulse is modeled as an isolated 500 attosecond pulse with a $\sin^2$ envelope centered at 27.21 eV and with an intensity of 1.6×10^{10} W/cm^2. The 40 fs NIR pulse is centered at 800 nm with an intensity of 1.5×10^{12} W/cm^2. The MCTDHF calculation produces the many-electron wave function $|\Psi(t)\rangle$ both during and after the pulses.

To describe the resulting spectrum, we start from a familiar expression for the transient absorption spectrum. If the time-dependent Hamiltonian is written as $\hat{H} = \hat{H}_0 - \hat{d}\,\mathcal{E}(t)$, where $\hat{H}_0$ is the field-free Hamiltonian, $\hat{d}$ is the dipole operator, and $\mathcal{E}(t)$ is the electric field of the applied XUV and NIR laser pulses, the single-molecule absorption spectrum is proportional to the response function [51–53], namely,

$$\tilde{S}(\omega) = 2\,\mathrm{Im}[\tilde{d}(\omega)\tilde{\mathcal{E}}^*(\omega)]. \tag{2}$$

In this equation, $\tilde{d}(\omega)$ and $\tilde{\mathcal{E}}(\omega)$ are the Fourier transform of the time-dependent induced dipole, $d(t) = \langle\Psi(t)|\hat{d}|\Psi(t)\rangle$, and the total applied electric field, $\mathcal{E}(t)$, respectively. We use the response function in this study together with *ab initio* calculations of the electron dynamics to compute the transient absorption signals. Equation (2) is also the point of departure for our description of these spectra using the simple models described in Sec. V. In both cases these spectra are used to compute the experimentally measured OD by employing the Beer-Lambert law as described in Appendix B where additional details of the MCTDHF calculations are given.

A number of previous calculations and experiments, for example, Refs. [32,54–58], considered only parallel polarization between the oxygen molecule internuclear axis and the XUV field, and thus invoked only two Rydberg series with $ns\sigma_g(^3\Sigma_u^-)$ $(l = 0, m = 0)$ character and with $nd\sigma_g(^3\Pi_u)$ $(l = 2, m = 0)$ character. In the MCTDHF calculation, as in the Schwinger variational calculation, we have assumed randomly oriented molecules in the presence of a linearly polarized XUV field in the calculation. Here again, therefore, in addition to Rydberg series corresponding to excitations from $2\sigma_u$ to $ns\sigma_g$ and $nd\sigma_g$ Rydberg orbitals, we found contributions from the third Rydberg series corresponding to excitations to orbitals with $nd\pi_g$ $(l = 2, m = 1)$ character, converging to the same limit and forming O_2 states of overall $^3\Pi_u$ symmetry.

Figure 3(b) shows MCTHDF calculations of the transient absorption spectra at a few representative time delays. It agrees well with experimental spectra in Fig. 3(a), and all $nd\sigma_g$ states show a dip in the transient absorption line shapes, while $(n+1)s\sigma_g$+$nd\pi_g$ states show a peak. Experimental line shapes exhibit more features than MCTDHF results due to the presence of transient absorption signals from an additional vibrational level $(\nu = 1)$ for each state, and this possibility is not considered in the MCTDHF calculation.

C. Comparison of experimental and MCTDHF spectrograms

Next, we compare full experimental and calculated spectrograms as shown in Figs. 5(a) and 5(c), respectively. The MCTDHF calculation generally agrees with the experimental data very well, where they both show alternative positive (red) and negative (blue) absorbance structures at $(n+1)s\sigma_g$ (including $nd\pi_g$) and $nd\sigma_g$ states, respectively. Moreover, the upward curve of absorption structure indicates that there are ac Stark shifts of the quasibound states induced by moderate strong NIR laser field. The observed Stark shift ~20 meV near zero delay corresponds well with the NIR laser peak intensity

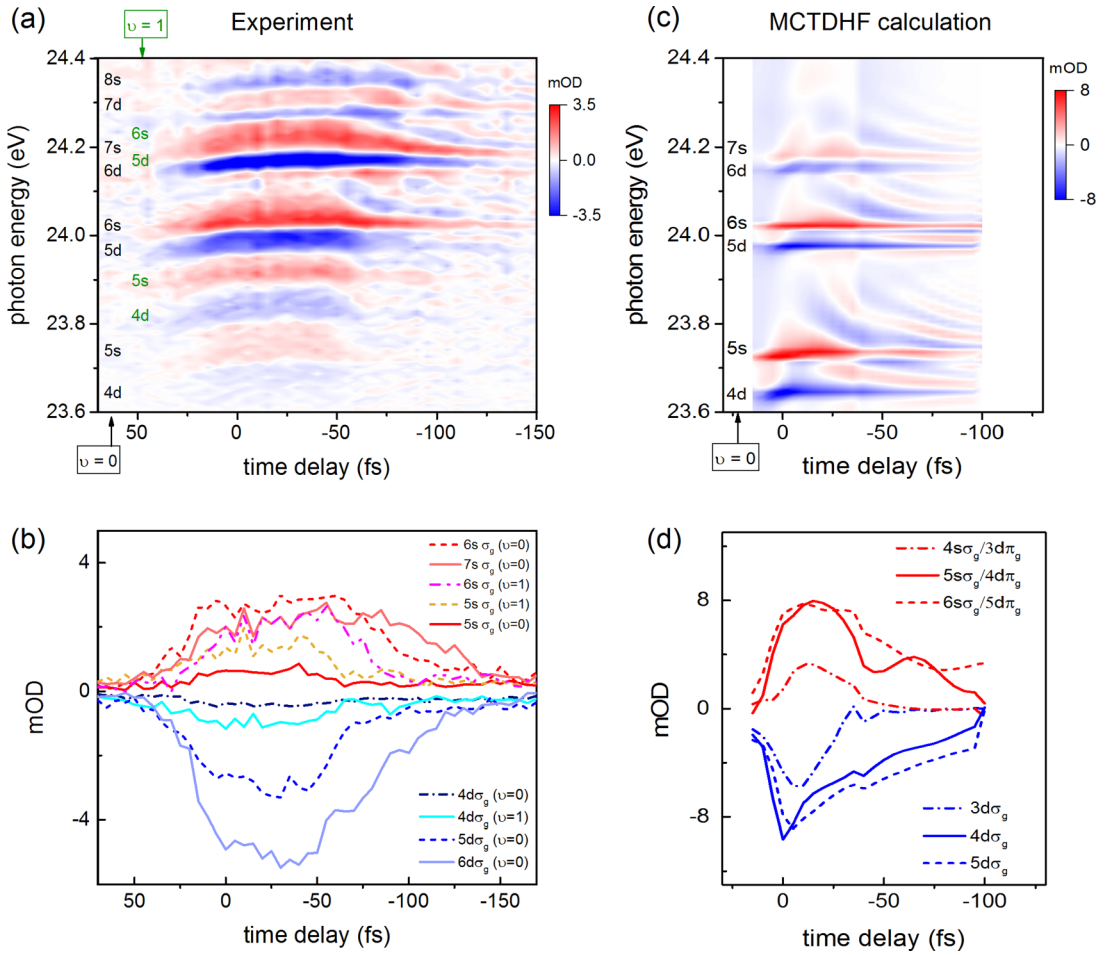

FIG. 5. (a) Measured transient absorption spectrogram labeled with various electronic states corresponding to $\nu = 0$ (black) and $\nu = 1$ (green) vibrational levels, and (b) its corresponding horizontal line-outs at some representative energy levels. (c) MCTDHF calculated transient absorption spectrogram and (d) its corresponding horizontal line-outs.

used. Also, hyperbolic fringes apparent at large negative time delays can be understood by the perturbed free induction decays, as also observed in ATAS studies in atomic gases. As mentioned earlier, experimental data contains contributions from $\nu = 1$ vibrational levels; therefore, the experimental spectrogram has more features than the theoretical counterpart.

By taking line-outs from the spectrograms at the energy location of various Rydberg states, we can obtain information about the evolution of these states. In Fig. 5(b), we take line-outs at the energies corresponding to the $4d(\nu = 0)$, $5s(\nu = 0)$, $4d(\nu = 1)$, $5s(\nu = 1)$, $5d(\nu = 0)$, $6s(\nu = 0)$, $6d(\nu = 0)$, $5d(\nu = 1)$, $7s(\nu = 0)$, $6s(\nu = 1)$, $7d(\nu = 0)$, and $8s(\nu = 0)$ states, in order of increasing energy, at the position of maximum positive or negative OD change. Note that the line-outs labeled $(n + 1)s\sigma_g$ include contributions from $nd\pi_g$. It is clear that regardless of the sign of the OD change the lifetime of polarization increases with the quantum number of the Rydberg series members. It is known that the natural autoionization lifetimes scale with effective quantum number as $(n^*)^3$ [59], and for each n, the $(n + 1)s\sigma_g$, $nd\pi_g$, and $nd\sigma_g$ states have similar n^* values (see Fig. 4), and have similar decay time scales.

It should be noted that the decay time scales observed here are faster than the autoionization lifetimes due to NIR pulse induced broadening of resonances [60]. Fitting a convolution of Gaussian and exponential decay to the evolution of $5d$, $6s(\nu = 0)$ signals, we obtain a decay time scale ~60 fs, corresponding to a net linewidth of ~11 meV. Subtracting the field-free natural linewidth of 3.6 meV (Table I), we estimate the effective NIR induced broadening of these resonances to be ~7 meV. The decay time scales for other $\nu = 0$ resonances are difficult to estimate as the transient absorption signals are either very weak or they overlap with vibrationally excited, $\nu = 1$ members of the Rydberg series. It is also hard to discern if decay time scales for $\nu = 1$ states are different from the $\nu = 0$ states. This is significant as the dissociation lifetime of $\nu = 1$ states are much shorter (~67 fs) than $\nu = 0$ dissociation lifetime (>ps), and thus can be comparable to autoionization lifetime [61] over the range of the effective quantum numbers considered here. One could argue in this case that as the molecule breaks up into excited atomic fragments, the decay of atomic polarization follows a similar trend as the original molecular polarization.

Figure 5(d) shows MCTDHF calculation line-outs for certain $ns(\nu = 0)$ and $nd(\nu = 0)$ states, and the trends in their lifetimes qualitatively agree with experimental observations and expectations that the larger effective quantum number states have longer autoionization lifetimes. However, our

MCTDHF calculations are not able to accurately reproduce the absolute lifetimes of these states, particularly those with higher principal quantum number. It should be noted that unlike some recent studies on excited states of H_2 [62], our experiment-theory comparison shows that for Rydberg autoionizing states in O_2 neither nuclear vibration nor molecular rotation has a significant effect on the delay-dependent line shapes obtained in transient absorption spectra.

V. FEW-LEVEL MODELS FOR TRANSIENT ABSORPTION SPECTRA

Transient absorption line shapes carry information about the XUV induced dipole polarization and its modification by an NIR pulse. For autoionizing states, we can use a few-level model to understand the origin of the correlation observed here between changes in the OD seen in transient absorption and Fano q parameters of the line shapes in the corresponding static XUV absorption spectrum. The central idea is to begin with a model for the polarization $d(t)$ induced by the XUV pulse that is capable of reproducing the Fano line shapes of the XUV spectrum, and then allow the NIR pulse to modify it by either laser-induced attenuation or laser-induced phase shift. We then use the modified $d(t)$ characterized by the time delay t_d, namely, $d_{t_d}(t)$, to calculate the change of the response function of Eq. (2), i.e., $\tilde{S}(\omega,t_d) - \tilde{S}(\omega)$, and therefore the transient absorption spectrum.

In the model system, an XUV interaction directly couples the ground state, $|g\rangle$, to both an excited metastable quasibounded (autoionizing) state, $|b\rangle$, and the background continuum at nearby energies, $|E\rangle$. A schematic of the energy levels in our few-level model system is shown in Fig. 6. A similar treatment of autoionizing states using a few-level model has been described in detail by Chu and Lin [53], and we generally follow their approach. For the diagram in Fig. 6, the time-dependent wave function of the system is a superposition of these states

$$\Psi(t) = e^{-iE_g t} C_g(t)|g\rangle + e^{-i(E_g+\omega_{\rm XUV})t} \times \left[C_b(t)|b\rangle + \int dE\, C_E(t)|E\rangle \right]. \quad (3)$$

The time-dependent coefficients $C_g(t)$, $C_b(t)$, and $C_E(t)$ can be computed by solving the corresponding time-dependent Schrödinger equation in which the time-dependent Hamiltonian is

$$\hat{H}(t) = \hat{H}_0 - \hat{d}[\mathcal{E}_{\rm XUV}(t) + \mathcal{E}_{\rm NIR}(t;t_d)], \quad (4)$$

where $\hat{H}_0$ is the unperturbed molecular Hamiltonian and $\hat{d}$ is the dipole operator. The XUV field, $\mathcal{E}_{\rm XUV}(t)$, is centered at $t = 0$, and the delayed NIR field is centered at $t = t_d$, so that

$$\mathcal{E}_{\rm NIR}(t;t_d) = \mathcal{E}^0_{\rm NIR} e^{-(t-t_d)^2/\tau^2_{\rm NIR}} e^{i\omega_L(t-t_d)} + \text{c.c.}, \quad (5)$$

where $\mathcal{E}^0_{\rm NIR}$ is the NIR peak field amplitude and $\hbar\omega_L$ is the NIR photon energy.

We first consider the case with XUV pulse alone to verify that this simple treatment with two discrete levels and a background continuum can describe the Fano profiles of autoionizing states. The ultrashort XUV field creates a polarization, $d(t)$, at the beginning of the XUV pulse,

$$d(t) = \langle \Psi(t)|\hat{d}|\Psi(t)\rangle. \quad (6)$$

We can solve for $|\Psi(t)\rangle$ and construct an analytic expression for $d(t)$ under the assumptions explained in Appendix C. We generalize the δ function XUV pulse used in [53] to have a Gaussian shape instead, with envelope function $F(t)$ and electric-field amplitude $F_{\rm XUV}$:

$$\mathcal{E}_{\rm XUV}(t) = F(t)\exp(i\omega_{\rm XUV}t) + \text{c.c.},$$
$$F(t) \equiv F_{\rm XUV} e^{-(t/\tau_{\rm XUV})^2}/\sqrt{\pi\tau^2_{\rm XUV}}. \quad (7)$$

The analytical expression for $d(t)$ due to this XUV pulse is given in Appendix C in Eq. (C13). In our model calculations, the XUV pulse width $\tau_{\rm XUV}$ is 5 fs. In the limit that the XUV pulse is infinitely narrow ($\tau_{\rm XUV} \to 0$) this pulse becomes a δ function pulse as used in [53].

In that limit this model produces precisely the Fano line shape of an absorption feature corresponding to the bound state, $|b\rangle$, embedded in the continuum as shown in Eq. (C9). Thus our point of departure for the simple models for how the line shapes of the pure XUV spectrum are modified by transient absorption is the assumption that the NIR pulse arriving at time delay t_d modifies the form of $d(t)$ initiated by the XUV pulse. In these models, the decay lifetimes and Fano q parameters are chosen so that the simulated frequency-domain static line shapes in Fig. 7(a) for $(5d,6s)$ states agree with our static photoabsorption cross section data in Fig. 1(b).

To model the NIR perturbation of XUV induced polarizations in the atomic case, two approaches are widely used: the laser-induced attenuation (LIA) model and laser-induced phase (LIP) model. The key assumption of the LIA model is that the intense NIR pulse extinguishes the polarization initiated by the XUV pulse by truncating the oscillating electric dipole. Its physical meaning is that the quasibound state population is depleted by the NIR pulse through transfer to other states and continua. In the sudden version of this approximation, the polarization can be expressed as

$$d_{t_d}(t) = \begin{cases} d(t), & t < t_d, \\ 0, & t \geqslant t_d, \end{cases} \quad \text{LIA model.} \quad (8)$$

A slower truncation can also be applied by using a smoother function for transition between two regimes. The LIA approach is central to a number of models for ATAS studies in many atomic gases [53,63–65].

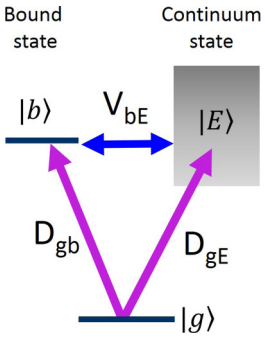

FIG. 6. Three-level model system showing a ground state $|g\rangle$, an excited bound state $|b\rangle$, and a continuum state $|E\rangle$, along with dipole couplings D_{gb}, D_{gE}, and interaction term V_{bE}.

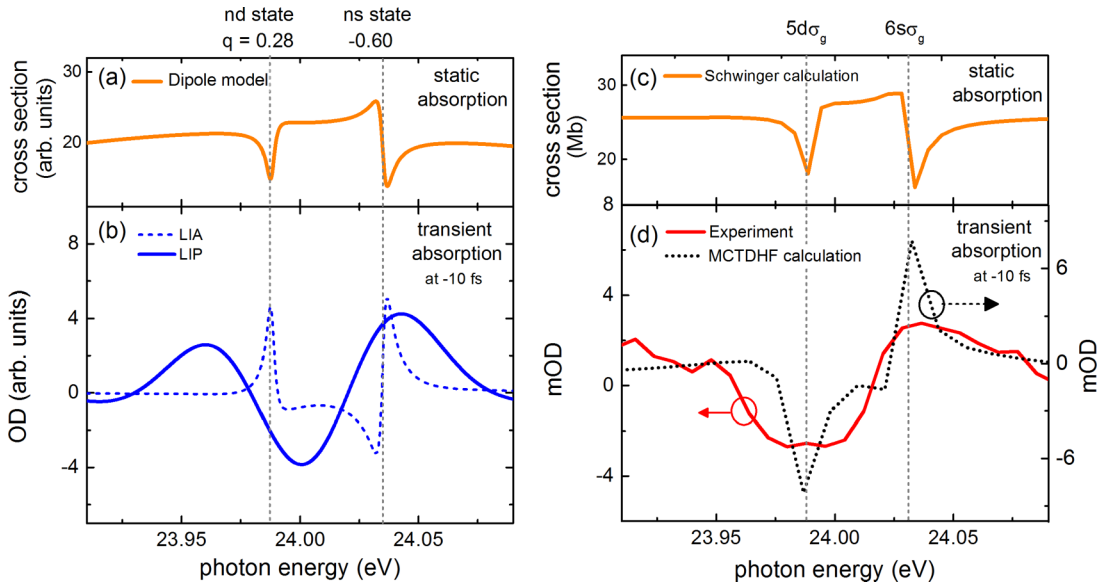

FIG. 7. Modeling of transient absorption line shapes resulting from the NIR perturbation. (a) Simulated static absorption profile that mimics the 5*d* and 6*s* state line shapes and the corresponding Fano *q* parameters. (b) Transient absorption spectra obtained when NIR perturbation is modeled as laser-induced phase (LIP) and laser-induced attenuation (LIA). (c) Calculated static absorption spectrum for 5*d* and 6*s* states based on Schwinger variational approach from Fig. 1(b) for comparison. (d) Experimentally measured transient absorption spectrum (solid red line), and MCTDHF calculated transient absorption spectrum (dashed black line) from Fig. 3(b) for comparison.

On the other hand, the LIP model assumes that the NIR field leads to an energy modification, $\Delta E(t,t_d)$, of the excited state, and hence the polarization will gain additional phase such that

$$d_{t_d}(t;t_d) = d(t)e^{i\phi(t,t_d)} \quad \text{LIP model,} \tag{9}$$

where the additional phase is $\phi(t,t_d) = \Delta E(t,t_d)t/\hbar$, and it depends on the delay time t_d of the NIR pulse. The LIP model has also been used to explain results of ATAS in many atomic cases [21,24,37,66].

Two methods can be used to calculate the energy and hence phase shift $\phi(t;t_d)$. References [24,66] calculate it based on the Stark energy shift, which is time-averaged and approximated as a pondermotive energy shift. Alternately, second-order perturbation theory can be used to calculate the energy shift in the presence of coupling to nearby states [21]. Here we took the former approach for the phase-shift calculation, and parametrized the pondermotive energy shift in atomic units as

$$E_{\text{pon}}(t;t_d) = \left[\mathcal{E}^0_{\text{NIR}} e^{-(t-t_d)^2/\tau^2_{\text{NIR}}}\right]^2 \Big/ \left(4\omega_L^2\right). \tag{10}$$

Thus the NIR modified dipole polarization becomes

$$d_{t_d}(t;t_d) = d(t)e^{i\,E_{\text{pon}}(t;t_d)\,t}. \tag{11}$$

Using either the LIP or LIA model, we Fourier transformed the modified polarization and calculated the response function using Eq. (2), thereby obtaining the OD as a function of energy and delay using Eq. (B2). Further details of our model calculations are given in Appendix C.

In the LIA model, we use smooth truncation of the XUV initiated polarization, which results in the absorption spectrum shown as the dashed blue line of Fig. 7(b) (at delay −10 fs). In this model, the absorption at the resonance energy increases or decreases depending on whether the absolute value of the Fano *q* parameter of the static line shape is either less than or greater than unity, similar to the behavior for a sudden truncation case exhibited explicitly in Eq. (C19). The Fano *q* parameters of the pairs of autoionizing features in static absorption spectrum [Fig. 1(b)] both have $|q| < 1$, but with differing signs, and thus the LIA model, even with gradual attenuation, fails to reproduce the directions of absorption changes observed in the transient absorption spectrum.

Using Fano *q* parameters from the static absorption profile in Fig. 7(a) and our experimental NIR pulse parameters, we also applied the LIP model with ponderomotive energy shift as a NIR perturbation effect, and results are shown in the solid blue line in Fig. 7(b). The application of a laser-induced phase evidently produces an effect in which the absorption increases or decreases depending on the *sign* of *q* when $|q| < 1$. For comparison of our model with full theory and the experiment, we show static absorption line shapes obtained using Schwinger calculation in Fig. 7(c). Figure 7(d) shows the transient absorption line shapes obtained experimentally (solid red line) and from MCTDHF calculation (solid black line) at a delay of −10 fs. Both our experimental and MCTDHF calculated line shapes agree well with the LIP model. It is important to note that the detailed measurements of complex line shapes associated with molecular polarization of pairs of *nd* and *ns* states provide the required detail to distinguish between the validity of different models. Based on our results, it seems that in this case the LIP assumptions better reflect the physics of ATAS experiment than those of the LIA model, even with smooth attenuation functions.

VI. CONCLUSION

In summary, we used the ATAS to investigate XUV initiated oxygen molecular polarization of superexcited states,

perturbed by a NIR pulse, and the alternate negative and positive absorption spectra for $nd\sigma_g$ and $(n+1)s\sigma_g$ autoionizing states are observed. The numerical results obtained using *ab initio* MCTDHF calculations agree with the experimental findings. In addition, from our MCTDHF and Schwinger variational calculations, we identify and include the contribution of a weaker $nd\pi_g$ state that overlaps with $(n+1)s\sigma_g$ state. From the transient absorption spectrograms, we observe that decay lifetimes of the dipole polarization for $nd\sigma_g$ and $(n+1)s\sigma_g$ states are similar and they increase with the effective quantum number n^*. However, the decay time scale is faster than the natural autoionization time scale due to NIR pulse induced broadening of resonances. The decay lifetime is also found to be insensitive to the vibrational state of the molecule, within the sensitivity of our measurements. To better interpret our findings, two models of NIR perturbation of the XUV initiated molecular polarization are tested against experimental and MCTDHF calculated transient absorption line profiles, and we find that laser-induced phase-shift model explains our results, while laser-induced attenuation does not. On these grounds, we conclude that the negative-positive transient absorption signals for nd/ns states can be explained in terms of two very different manifestations of electronic interference in molecular excitation (opposite signs of initial Fano q parameters) influenced by the same NIR induced Stark shift in transient absorption experiments. We envision that additional ATAS investigations of low quantum number Rydberg states that do not follow core-ion approximation [57], with few-cycle NIR pulses, will enable us to study the nonadiabatic effects associated with fast autoionization and dissociation in O_2. The relationship between the static properties and transient absorption line shapes explored here leads us to propose that finer features of ATAS spectra in molecules could be used to characterize the undetermined electronic properties of dynamically evolving systems and test the theoretical models of the strong-field modification of the correlated electron dynamics, including recently proposed interference stabilization of autoionizing states [67].

ACKNOWLEDGMENTS

Work at the University of Arizona and the University of California Davis was supported by the U. S. Army Research Laboratory and the U. S. Army Research Office under Grant No. W911NF-14-1-0383. Work performed at Lawrence Berkeley National Laboratory was supported by the U. S. Department of Energy Office of Basic Energy Sciences, Division of Chemical Sciences Contract No. DE-AC02-05CH11231. Work at Texas A&M University was supported by US DOE Basic Energy Sciences Grant No. DE-SC0012198. C.-T.L. acknowledges support from Arizona TRIF Photonics Fellowship.

C.-T.L and X.L. contributed equally to this work in the form of experimental and theoretical effort, respectively.

APPENDIX A: EXPERIMENTAL SETUP

A Ti:sapphire laser amplifier is used to produce 40 fs NIR pulses at 1 kHz repetition rate with pulse energy 2 mJ and central wavelength 780 nm, with no active control of carrier envelope phase. After exiting the amplifier, the NIR pulse is divided into two paths. The NIR pulse on the first path is focused into a xenon gas filled hollow-core capillary waveguide to generate XUV APT with ~440 attosecond bursts and ~4 fs envelope via the HHG process. The APT is dominated by harmonics 13, 15, and 17. The harmonic XUV beam is passed through an aluminum filter to remove residual NIR, and then a toroidal mirror is used to focus the XUV into a gas cell, which constitutes our interaction region. The 15th harmonic in the XUV beam is resonant with neutral superexcited states of oxygen and initiates the molecular polarization. The delayed NIR pulse on the second path passes through a focusing lens, and it is recombined collinearly with XUV beam using a mirror with a hole. Both XUV and NIR pulses impinge on a 1 cm length oxygen gas cell with a backing pressure of 4 torr, with aluminum foils providing gas to vacuum partition. The NIR pulse, with focused peak intensity at ~1 TW/cm^2, drills through covering foils, allowing both XUV and NIR beams to propagate forward collinearly towards an XUV spectrometer.

A homemade XUV spectrometer is used, which includes a concave grating (1200 lines/mm, 1 m radius of curvature) and a back-illuminated thermoelectric-cooled x-ray CCD camera. Another 200-nm-thick aluminum filter is equipped in front of the camera to block NIR. We use a shutter in the NIR delay line to obtain background (NIR free) XUV only spectra $I_{\rm out}^{\rm XUV}$ at each camera exposure. The spectrometer detects transmitted XUV spectra with a resolution of ~10 meV at 24 eV. The spectrometer does not resolve the narrow NIR-free oxygen absorption lines; therefore, the transmitted XUV spectrum $I_{\rm out}^{\rm XUV}$ in the absence of NIR field is essentially the same as the input XUV spectrum $I_{\rm in}^{\rm XUV}$. We use it as a reference in OD measurements. The experimental OD is obtained from near-simultaneously measured transmitted XUV spectrum with NIR present, and without NIR, with 0.1 s exposure time per camera exposure. The absolute values of experimental OD are shifted slightly lower due to the presence of residual camera background in the raw data, and this effect can be significant at photon energies where XUV intensity is very low. We averaged 200 camera frames at each delay step and the statistical error bars on our data range from ± 1 to 2 mOD.

APPENDIX B: MCTDHF METHOD

To calculate the transient absorption spectra, we applied the MCTDHF method, which simultaneously describes stable valence states, core-hole states, and the photoionization continuua. MCTDHF implementation solves the time-dependent Schrödinger equation in full dimensionality, and because it is based on a combination of the discrete variable representation (DVR) and exterior complex scaling (ECS) of the electronic coordinates, it rigorously treats the ionization continua for both single and multiple ionization. As more orbitals are included, the MCTDHF wave function formally converges to the exact many-electron solution. The MCTDHF electronic wave function is described by an expansion in terms of time-dependent Slater determinants, $|\Psi(t)\rangle = \sum_a A_a(t)|\vec{n}_a(t)\rangle$, in which each determinant is the antisymmetrized product of N spin orbitals, $|\vec{n}_\alpha(t)\rangle = \mathscr{A}(|\phi_{a1}(t)\rangle \cdots |\phi_{aN}(t)\rangle)$. These

spin-restricted orbitals $|\phi_a(t)\rangle$ are in turn expanded in a set of time-dependent discrete DVR basis functions, and full configuration interaction is employed within the electronic space. We reach the MCTDHF working equations by applying the Dirac-Frenkel variational principle to the time-dependent Schrödinger equation for the trial function. Details of the resulting working equations and their solution can be found in Ref. [68].

The results presented here were calculated using nine orbitals, which can be labeled as σ_g, σ_g, σ_u, σ_u,$\pi_{u,\pm1}$, σ_g, $\pi_{g,\pm1}$ at the beginning of the propagation. These calculations have a spin adapted triplet configuration space of dimension 36. We used a fixed nuclei Hamiltonian where the internuclear distance is 2.282 bohr. Prolate spheroidal coordinates, (η,ξ,ϕ), were used in these calculations, and we employ a DVR grid of 10 points for η and a ξ grid with twelve grid points per finite element. Nine finite elements were used in ξ, the first of length $2.0a_0$ providing a dense grid to represent the 1 s orbital and orbital cusp region, with seven subsequent five elements of length $8.0a_0$. Exterior complex scaling is applied to the remaining four elements extending an additional $32a_0$ with a complex scaling angle of 0.40 radians. The results show no sensitivity to the ECS angle, indicating that all ionized flux is being completely absorbed by the ECS procedure.

The MCTDHF calculation describes the relative energies and line shapes in these cross sections, but does not reproduce the absolute excitation energies of these autoionizing states. Thus the calculated results were shifted to lower energies by 5.18 eV such that the limit of the calculated Rydberg series, corresponding to the $c\,^4\Sigma_u^-$ state of $O_2{}^+$, agrees with the literature value. Because the present calculations used a fixed-nuclei treatment, the MCTDHF computed cross section does not exhibit vibrational structure. We observe that the relative energies of the $(2\sigma_u)^{-1}(ns\sigma_g)$ and $(2\sigma_u)^{-1}(nd\sigma_g)$ series from our fixed-nuclei MCTDHF calculations agree well with the locations of first vibrational states ($\nu = 0$) of those two series as in [31,32].

The MCTDHF computed cross section is for randomly oriented molecules in the presence of a linearly polarized XUV field. This total cross section is computed using the appropriate relation for single photon absorption, $\sigma_{\text{total}} = \frac{1}{3}\sigma_\parallel + \frac{2}{3}\sigma_\perp$, where $\sigma_\parallel$ and $\sigma_\perp$ are calculated separately for oriented molecules either parallel or perpendicular to the polarization directions of the fields. The calculations from Demekhin *et al.* [32] considered only parallel polarization, and thus there were only two Rydberg series, $(2\sigma_u)^{-1}(ns\sigma_g)$ and $(2\sigma_u)^{-1}(nd\sigma_g)$, converging to the $c\,^4\Sigma_u^-$ limit. However, using perpendicular polarization, the MCTDHF computed $\sigma_\perp$ exhibits a third Rydberg series converging to the same limit, namely, the series we have identified as $(2\sigma_u)^{-1}(nd\pi_g)$ here.

To compute quantities directly comparable to the experimental observation of the quantity in Eq. (1), we begin with Beer-Lambert law, $-\log_{10}[I_{\text{out}}/I_{\text{in}}] = \sigma\, N\, L$ where I_{in} and I_{out} are the incoming and outgoing field intensities, respectively, and σ is the photoabsorption cross section. For these comparisons, we estimated the molecular density as $N = 1 \times 10^{16}$ cm^{-3} and $L = 1$ cm for the path length. The photoabsorption cross section is related to the response functions, $\tilde{S}(\omega)$, computed using the MCTDHF method. Therefore, we can construct the appropriate OD corresponding

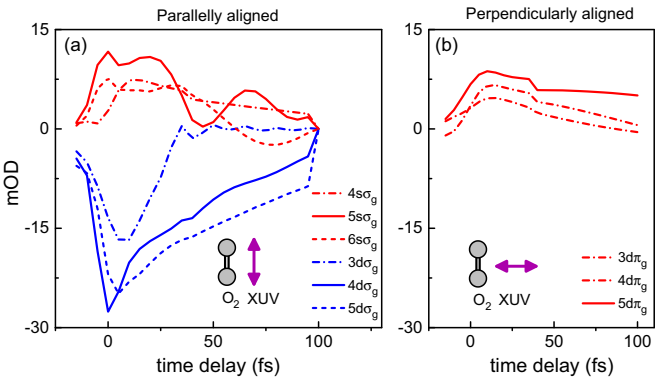

FIG. 8. Transient absorption line-outs calculated using MCTDHF method for molecules (a) aligned parallel to XUV field polarization, and (b) perpendicular to XUV field polarization, plotted at the energies corresponding to several resonances. Note that the NIR field polarization is always parallel to the XUV field polarization.

to Eq. (1) as

$$\begin{aligned}\text{OD} &= -\log_{10}\left[\frac{I_{\text{out}}^{\text{XUV+NIR}}(t_d)}{I_{\text{out}}^{\text{XUV}}}\right] \\ &= -\left\{\log_{10}\left[\frac{I_{\text{out}}^{\text{XUV+NIR}}(t_d)}{I_{\text{in}}^{\text{XUV+NIR}}}\right] - \log_{10}\left[\frac{I_{\text{out}}^{\text{XUV}}}{I_{\text{in}}^{\text{XUV}}}\right]\right\} \\ &= 4\pi\alpha\omega\left[\frac{\tilde{S}_{\text{XUV+NIR}}(\omega;t_d)}{\left|\tilde{\mathcal{E}}_{\text{in}}^{\text{XUV+NIR}}(\omega)\right|^2} - \frac{\tilde{S}_{\text{XUV}}(\omega)}{\left|\tilde{\mathcal{E}}_{\text{in}}^{\text{XUV}}(\omega)\right|^2}\right]NL. \quad \text{(B1)}\end{aligned}$$

At frequencies in the XUV, the contribution of the NIR pulse is negligible, so that $\tilde{\mathcal{E}}_{\text{in}}^{\text{XUV+NIR}}(\omega) \approx \tilde{\mathcal{E}}_{\text{in}}^{\text{XUV}}(\omega)$. With that assumption, Eq. (B1) becomes the following working expression for the measured quantity in terms of the calculated frequency- and delay-dependent response functions:

$$\text{OD} \approx 4\pi\alpha\omega\frac{[\tilde{S}_{\text{XUV+NIR}}(\omega;t_d) - \tilde{S}_{\text{XUV}}(\omega)]}{\left|\tilde{\mathcal{E}}_{\text{in}}^{\text{XUV}}(\omega)\right|^2}NL. \quad \text{(B2)}$$

When the molecular axis of O_2 is parallel to both XUV and NIR field polarization directions as in Fig. 8(a), the $nd\sigma_g$ states exhibit negative OD, while $ns\sigma_g$ states show positive OD. However, as shown in Fig. 8(b), where the molecular axis is perpendicular to the polarization directions of both XUV and NIR fields, the $nd\pi_g$ states contribute positive OD. In order to compute the time-delay dependent OD for randomly oriented molecules, we make the approximation (exact for one-photon absorption), $\text{OD}_{\text{total}} = \frac{1}{3}\text{OD}_\parallel + \frac{2}{3}\text{OD}_\perp$, and the result is shown in Figs. 3(b) and 5(d). Specifically, in Fig. 5(d) we show OD at six energies which correspond to three resonances for the $(2\sigma_u)^{-1}nd\sigma_g$ series, and three resonances for the $(2\sigma_u)^{-1}(nd\pi_g) + (2\sigma_u)^{-1}(ns\sigma_g)$ series.

APPENDIX C: FEW-LEVEL MODEL FOR TRANSIENT ABSORPTION

1. XUV initiated polarization

We first substitute Eq. (3) and the Hamiltonian in Eq. (4) into the Schrödinger equation, and then project onto that equation with $\langle g|$, $\langle b|$, and $\langle E|$. We then assume that the

only nonzero dipole matrix elements are $D_{gb} = \langle g|\hat{d}|b\rangle$ and $D_{gE} = \langle g|\hat{d}|E\rangle$, and recalling that the XUV field is $\mathcal{E}_{\rm XUV}(t) = F(t)e^{i\omega_{\rm XUV}t}$ + c.c., make the rotating wave approximation. We also assume that the molecular Hamiltonian, H_0, couples only $|b\rangle$ to $|E\rangle$, so that its only nonzero matrix elements are $E_g = \langle g|H_0|g\rangle$, $E_b = \langle b|H_0|b\rangle$, $\langle E|H_0|E'\rangle = \delta(E - E')$, and $V_{bE} = \langle b|H_0|E\rangle$. Then, using the orthogonality of $|g\rangle$, $|b\rangle$, and $|E\rangle$, we find that the time-dependent coefficients $C_g(t)$, $C_b(t)$, and $C_E(t)$ satisfy the coupled differential equations,

$$i\dot{C}_g = -\left[\int dE\, D_{gE}C_E F(t) + D_{gb}C_b F(t)\right], \quad \text{(C1)}$$

$$i\dot{C}_b = [E_b - (E_g + \omega_{\rm XUV})]C_b + \int dE\, V_{bE}C_E - D^*_{gb}C_g F(t)^*, \quad \text{(C2)}$$

$$i\dot{C}_E = [E - (E_g + \omega_{\rm XUV})]C_E + V_{Eb}C_b - D_{Eg}C_g F(t)^*. \quad \text{(C3)}$$

We also adopt the adiabatic elimination of the continuum by assuming that the coefficients of the continuum states change much more slowly than those of the discrete states, i.e., $\dot{C}_E \approx 0$, as was done in Ref. [53]. The equation for the time-dependent coefficients for the continuum states, $C_E(t)$, can thus be simplified to give

$$C_E = -\frac{V_{Eb}C_b - D_{Eg}C_g F(t)^*}{E - (E_g + \omega_{\rm XUV})}. \quad \text{(C4)}$$

The coefficient $C_E(t)$ appears in the coupled equations under the integration $\int dE$ over continuum states, so this equation is actually a representation of a Green's function, namely,

$$C_E = \lim_{\epsilon\to 0^+} \frac{V_{Eb}C_b - D_{Eg}C_g F(t)^*}{(E_g + \omega_{\rm XUV}) - E + i\epsilon}. \quad \text{(C5)}$$

We then retain only the resonant contribution to the integral over E in Eq. (C1) and the next equation, i.e., the contribution is proportional to $-i\pi\delta(E_g + \omega_{\rm XUV} - E)$. Making use of the definitions of the Fano q parameter, we arrive at simplified equations for $C_g(t)$ and $C_b(t)$ for the discrete states,

$$i\dot{C}_g = -i\pi|D_{gE}|^2|F(t)|^2C_g - D_{gb}C_b F(t)(1 - i/q), \quad \text{(C6)}$$

$$i\dot{C}_b = [\Delta_b - i\Gamma/2]C_b - D^*_{gb}C_g F(t)^*(1 - i/q), \quad \text{(C7)}$$

with D_{gE} evaluated at $E = E_g + \omega_{\rm XUV}$ and $\Delta_b = E_b - (E_g + \omega_{\rm XUV})$. Here, q and Γ are the conventionally defined Fano q parameters that describe the line shape and the width,

$$q = \frac{D_{gb}}{\pi D_{gE}V_{Eb}}, \quad \text{(C8)}$$

$$\Gamma = 2\pi|V_{Eb}|^2. \quad \text{(C9)}$$

Going back to the original expression for the $\Psi(t)$ in Eq. (3), we can express the leading contribution to the time-dependent dipole as

$$\begin{aligned} d(t) &\equiv \langle\Psi(t)|\hat{d}|\Psi(t)\rangle \\ &= \exp(-i\omega_{\rm XUV}t)C^*_g\left[D_{gb}C_b + \int dE\, D_{gE}C_E\right] + \text{c.c.} \\ &= \exp(-i\omega_{\rm XUV}t)[C^*_g D_{gb}C_b(1 - i/q) \\ &\quad + i\pi|C_g|^2|D_{gE}|^2F(t)^*] + \text{c.c.} \end{aligned} \quad \text{(C10)}$$

So we need only $C_g(t)$ and $C_b(t)$ to evaluate this expression. We now make the approximation that the ground state is not appreciably depopulated, $C_g(t) \approx 1$, note also that on resonance $\Delta_b = 0$, and solve the equation for C_b using the substitution $C_b = \exp(-\Gamma t/2)\,\tilde{C}_b$ in the case of the Gaussian XUV pulse in Eq. (7) to obtain

$$C_b(t) = i\,e^{-\Gamma t/2}D^*_{gb}(1 - i/q)F_{\rm XUV}G(t), \quad \text{(C11)}$$

where we define

$$G(t) \equiv \tfrac{1}{2}\,e^{\Gamma^2\tau^2_{\rm XUV}/16}[1 + \text{erf}\,(\Gamma\tau_{\rm XUV}/4 + t/\tau_{\rm XUV})], \quad \text{(C12)}$$

and erf is the error function. Assembling $d(t)$ we then find

$$\begin{aligned} d(t) = e^{-i\omega_{\rm XUV}t}\big[&i|D_{gb}|^2(1 - i/q)^2F_{\rm XUV}\,G(t)\,e^{-\Gamma t/2} \\ &+ i\pi|D_{gE}|^2F_{\rm XUV}\,e^{-t^2/\tau^2_{\rm XUV}}\left(\pi\tau^2_{\rm XUV}\right)^{-1/2}\big] + \text{c.c.} \end{aligned} \quad \text{(C13)}$$

This is the expression for the polarization that we use to model transient absorption, by modifying it with either laser-induced attenuation or laser-induced phase shift as described in Sec. V, and then Fourier transforming it according to

$$\tilde{d}(\omega) = \frac{1}{\sqrt{2\pi}}\int_{-\infty}^{\infty} dt\, e^{i\omega t}d(t) \quad \text{(C14)}$$

to construct the response function in Eq. (2) that gives the transient absorption spectrum.

To make the connection with Fano line shapes in the pure XUV absorption spectrum we evaluate Eq. (C13) in the limit of a δ function XUV pulse, $\tau_{\rm XUV} \to 0$, so that

$$d(t) = \begin{cases} 0, & t < 0, \\ e^{-i\,\omega_{\rm XUV}t}[i|D_{gb}|^2(1 - i/q)^2F_{\rm XUV}e^{-\frac{\Gamma}{2}t} + i\pi|D_{gE}|^2F_{\rm XUV}\delta(t)], & t \geqslant 0, \end{cases} \quad \text{(C15)}$$

and the Fourier transform of the polarization becomes

$$\tilde{d}(\omega) = \frac{1}{\sqrt{2\pi}}F_{\rm XUV}\left[i\pi|D_{gE}|^2 - \frac{(1 - i/q)^2|D_{gb}|^2}{\omega - \omega_{\rm XUV} + i\,\Gamma/2}\right]. \quad \text{(C16)}$$

With this approximation to $\tilde{d}(\omega)$, and the Fourier transform of the corresponding XUV field, $\tilde{\mathcal{E}}_{\rm XUV}(\omega) = F_{\rm XUV}/\sqrt{2\pi}$, the absorption cross section now becomes

$$\sigma(\omega) = 8\pi\alpha\omega\,\text{Im}[\tilde{d}(\omega)/\mathcal{E}(\omega)] = 8\pi^2\alpha\,\omega|D_{gE}|^2\frac{(\omega - \omega_{\rm XUV} + q\,\Gamma/2)^2}{(\omega - \omega_{\rm XUV})^2 + (\Gamma/2)^2}, \quad \text{(C17)}$$

which has the well-known form of the absorption cross section in the vicinity of an autoionizing feature with a Fano resonance line shape. In this limit of a δ function XUV pulse, it is possible to analytically evaluate the Fourier transform of the modified $d(t)$ in the case of sudden attenuation in the LIA model in Eq. (8) and see explicitly how it depends on the Fano q parameters of the unperturbed line shape. The change in the response function due to this sudden truncation of the polarization is

$$\Delta\tilde{S}(\omega;t_d) \equiv \tilde{S}(\omega;t_d) - \tilde{S}_{\mathrm{XUV}}(\omega), \tag{C18}$$

and the final expression for $\Delta\tilde{S}(\omega;t_d)$ in this simple model, evaluated at the resonance energy $\omega = \omega_{\mathrm{XUV}}$, can then be shown to be

$$\Delta\tilde{S}(\omega=\omega_{\mathrm{XUV}};t_d) = |F_0|^2|D_{gE}|^2(1-q^2)e^{-\Gamma t_d/2}. \tag{C19}$$

As we can see from Eq. (C19) in this extreme version of the LIA model, the dependence on Fano q parameter of the change in the response function is negative or positive depending on whether q is greater or less than unity because of the factor of $1-q^2$ in Eq. (C19).

2. NIR perturbation: The LIA and LIP models

We can extend the above approach to set up two superimposed polarizations corresponding to a pair of features of $nd\sigma_g$ and $ns\sigma_g + nd\pi_g$, as the weighted sum of two polarizations $C_{nd}d^{nd}(t;q_{nd},\Gamma_{nd}) + C_{ns}d^{ns}(t;q_{ns},\Gamma_{ns})$. The polarization labeled d^{ns} includes $ns\sigma_g + nd\pi_g$ contributions, and the weighting coefficients C_{nd} and C_{ns} are chosen to reproduce static absorption spectrum as in our Schwinger calculation.

We then calculate the response function as defined in Eq. (2) in spectral domain. The parameters, such as Fano q, the field-free decay lifetimes Γ, and the amplitudes of dipole matrix elements D_{gb} and D_{bE}, are chosen so that the response function closely matches the static absorption line shapes shown in Fig. 1(b). The delay-dependent NIR perturbations are then modeled as LIA or LIP. In the LIA method, XUV initiated polarizations are attenuated slowly by an error function profile centered at some delay t_d to simulate the effect of excited-state population removal by a Gaussian shaped NIR pulse. The parameters used for the LIP calculations that determine the ponderomotive energy function were $\mathcal{E}^0_{\mathrm{NIR}} = 5.3\times10^{-3}$ a.u., corresponding to an intensity of 1 TWcm^2, and the NIR photon energy $\omega_L = 0.058$ a.u. (1.58 eV).

[1] U. Becker and D. A. Shirley, *VUV and Soft X-ray Photoionization* (Springer Science & Business Media, New York, 2012).
[2] C.-Y. Ng, *Vacuum Ultraviolet Photoionization and Photodissociation of Molecules and Clusters* (World Scientific, Singapore, 1991).
[3] R. L. Platzman, Radiat. Res. **17**, 419 (1962).
[4] Y. Hatano, Phys. Rep. **313**, 109 (1999).
[5] H. Nakamura, Int. Rev. Phys. Chem. **10**, 123 (1991).
[6] R. P. Wayne, *Chemistry of Atmosphere: An Introduction to the Chemistry of the Atmosphere of Earth, the Planets and Their Satellites* (Oxford, Clarendon, 1991).
[7] B. Boudaıffa, P. Cloutier, D. Hunting, M. A. Huels, and L. Sanche, Science **287**, 1658 (2000).
[8] A. Florescu-Mitchell and J. Mitchell, Phys. Rep. **430**, 277 (2006).
[9] V. Kokoouline, N. Douguet, and C. H. Greene, Chem. Phys. Lett. **507**, 1 (2011).
[10] N. Douguet, A. E. Orel, C. H. Greene, and V. Kokoouline, Phys. Rev. Lett. **108**, 023202 (2012).
[11] V. Kokoouline, C. H. Greene, and B. D. Esry, Nature (London) **412**, 891 (2001).
[12] S. L. Guberman and A. Giusti-Suzor, J. Chem. Phys. **95**, 2602 (1991).
[13] C. Jungen and S. T. Pratt, J. Chem. Phys. **133**, 214303 (2010).
[14] A. Rundquist, C. G. Durfee, Z. Chang, C. Herne, S. Backus, M. M. Murnane, and H. C. Kapteyn, Science **280**, 1412 (1998).
[15] P. Paul, E. Toma, P. Breger, G. Mullot, F. Augé, P. Balcou, H. Muller, and P. Agostini, Science **292**, 1689 (2001).
[16] E. Gagnon, P. Ranitovic, X.-M. Tong, C. L. Cocke, M. M. Murnane, H. C. Kapteyn, and A. S. Sandhu, Science **317**, 1374 (2007).
[17] A. S. Sandhu, E. Gagnon, R. Santra, V. Sharma, W. Li, P. Ho, P. Ranitovic, C. L. Cocke, M. M. Murnane, and H. C. Kapteyn, Science **322**, 1081 (2008).
[18] F. Krausz and M. Ivanov, Rev. Mod. Phys. **81**, 163 (2009).
[19] E. Goulielmakis, Z.-H. Loh, A. Wirth, R. Santra, N. Rohringer, V. S. Yakovlev, S. Zherebtsov, T. Pfeifer, A. M. Azzeer, M. F. Kling *et al.*, Nature (London) **466**, 739 (2010).
[20] H. Wang, M. Chini, S. Chen, C.-H. Zhang, F. He, Y. Cheng, Y. Wu, U. Thumm, and Z. Chang, Phys. Rev. Lett. **105**, 143002 (2010).
[21] M. Chini, B. Zhao, H. Wang, Y. Cheng, S. X. Hu, and Z. Chang, Phys. Rev. Lett. **109**, 073601 (2012).
[22] S. Chen, M. J. Bell, A. R. Beck, H. Mashiko, M. Wu, A. N. Pfeiffer, M. B. Gaarde, D. M. Neumark, S. R. Leone, and K. J. Schafer, Phys. Rev. A **86**, 063408 (2012).
[23] M. Holler, F. Schapper, L. Gallmann, and U. Keller, Phys. Rev. Lett. **106**, 123601 (2011).
[24] C. Ott, A. Kaldun, P. Raith, K. Meyer, M. Laux, J. Evers, C. H. Keitel, C. H. Greene, and T. Pfeifer, Science **340**, 716 (2013).
[25] C.-T. Liao, A. Sandhu, S. Camp, K. J. Schafer, and M. B. Gaarde, Phys. Rev. Lett. **114**, 143002 (2015).
[26] C.-T. Liao, A. Sandhu, S. Camp, K. J. Schafer, and M. B. Gaarde, Phys. Rev. A **93**, 033405 (2016).
[27] E. R. Warrick, W. Cao, D. M. Neumark, and S. R. Leone, J. Phys. Chem. A **120**, 3165 (2016).
[28] M. Reduzzi, W. Chu, C. Feng, A. Dubrouil, J. Hummert, F. Calegari, F. Frassetto, L. Poletto, O. Kornilov, M. Nisoli *et al.*, J. Phys. B **49**, 065102 (2016).
[29] A. E. Miroshnichenko, S. Flach, and Y. S. Kivshar, Rev. Mod. Phys. **82**, 2257 (2010).
[30] U. Fano, Phys. Rev. **124**, 1866 (1961).
[31] D. M. P. Holland, D. A. Show, and S. M. McSweeney, Chem. Phys. **173**, 315 (1993).
[32] P. V. Demekhin, D. V. Omel'yanenko, B. M. Lagutin, V. L. Sukhorukov, L. Werner, A. Ehresmann, K.-H. Schartner, and H. Schmoranzer, Opt. Spectrosc. **102**, 318 (2007).
[33] F. R. Gilmore, J. Quant. Spectrosc. Radiat. Transfer **5**, 369 (1965).

[34] P. Baltzer, B. Wannberg, L. Karlsson, M. Carlsson Göthe, and M. Larsson, Phys. Rev. A **45**, 4374 (1992).
[35] A. Ehresmann, L. Werner, S. Klumpp, H. Schmoranzer, P. V. Demekhin, B. Lagutin, V. Sukhorukov, S. Mickat, S. Kammer, B. Zimmermann *et al.*, J. Phys. B **37**, 4405 (2004).
[36] C. Ott, A. Kaldun, L. Argenti, P. Raith, K. Meyer, M. Laux, Y. Zhang, A. Blättermann, S. Hagstotz, T. Ding *et al.*, Nature (London) **516**, 374 (2014).
[37] M. Wu, S. Chen, S. Camp, K. J. Schafer, and M. B. Gaarde, J. Phys. B **49**, 062003 (2016).
[38] R. E. Stratmann and R. R. Lucchese, J. Chem. Phys. **102**, 8493 (1995).
[39] R. E. Stratmann, R. W. Zurales, and R. R. Lucchese, J. Chem. Phys. **104**, 8989 (1996).
[40] G. Bandarage and R. R. Lucchese, Phys. Rev. A **47**, 1989 (1993).
[41] J. Dunning and T. H. Dunning, J. Chem. Phys. **90**, 1007 (1989).
[42] R. A. Kendall, T. H. Dunning, and R. J. Harrison, J. Chem. Phys. **96**, 6796 (1992).
[43] C. R. Wu, J. Quant. Spectrosc. Radiat. Transfer **37**, 1 (1987).
[44] O. E. Alon, A. I. Streitsov, and L. S. Cederbaum, J. Chem. Phys. **127**, 154103 (2007).
[45] J. Caillat, J. Zanghellini, M. Kitzler, O. Koch, W. Kreuzer, and A. Scrinzi, Phys. Rev. A **71**, 012712 (2005).
[46] T. Kato and H. Kono, Chem. Phys. **366**, 46 (2009).
[47] I. S. Ulusoy and M. Nest, J. Chem. Phys. **136**, 054112 (2012).
[48] R. P. Miranda, A. J. Fisher, L. Stella, and A. P. Horsfield, J. Chem. Phys. **134**, 244101 (2011).
[49] H. Miyagi and L. B. Madsen, Phys. Rev. A **87**, 062511 (2013).
[50] T. Sato and K. L. Ishikawa, Phys. Rev. A **88**, 023402 (2013).
[51] D. J. Tannor, *Introduction to Quantum Mechanics: A Time Dependent Perspective* (University Science Press, Sausalito, 2007).
[52] M. B. Gaarde, C. Buth, J. L. Tate, and K. J. Schafer, Phys. Rev. A **83**, 013419 (2011).
[53] W.-C. Chu and C. D. Lin, Phys. Rev. A **87**, 013415 (2013).
[54] D. Cubric, A. Wills, J. Comer, and M. Ukai, J. Phys. B **26**, 3081 (1993).
[55] H. Liebel, S. Lauer, F. Vollweiler, R. Müller-Albrecht, A. Ehresmann, H. Schmoranzer, G. Mentzel, K.-H. Schartner, and O. Wilhelmi, Phys. Lett. A **267**, 357 (2000).
[56] H. Liebel, A. Ehresmann, H. Schmoranzer, P. V. Demekhin, B. Lagutin, and V. Sukhorukov, J. Phys. B **35**, 895 (2002).
[57] Y. Hikosaka, P. Lablanquie, M. Ahmad, R. Hall, J. Lambourne, F. Penent, and J. Eland, J. Phys. B **36**, 4311 (2003).
[58] B. Doughty, C. J. Koh, L. H. Haber, and S. R. Leone, J. Chem. Phys. **136**, 214303 (2012).
[59] H. Lefebvre-Brion and R. W. Field, *The Spectra and Dynamics of Diatomic Molecules* (Elsevier Inc., Amsterdam, 2004), p. 572.
[60] X. Li, B. Bernhardt, A. R. Beck, E. R. Warrick, A. N. Pfeiffer, M. J. Bell, D. J. Haxton, C. W. McCurdy, D. M. Neumark, and S. R. Leone, J. Phys. B **48**, 125601 (2015).
[61] A. Padmanabhan, M. MacDonald, C. Ryan, L. Zuin, and T. Reddish, J. Phys. B **43**, 165204 (2010).
[62] J. E. Bækhøj, L. Yue, and L. B. Madsen, Phys. Rev. A **91**, 043408 (2015).
[63] B. Bernhardt, A. R. Beck, X. Li, E. R. Warrick, M. J. Bell, D. J. Haxton, C. W. McCurdy, D. M. Neumark, and S. R. Leone, Phys. Rev. A **89**, 023408 (2014).
[64] A. N. Pfeiffer, M. J. Bell, A. R. Beck, H. Mashiko, D. M. Neumark, and S. R. Leone, Phys. Rev. A **88**, 051402 (2013).
[65] X. Li, B. Bernhardt, A. R. Beck, E. R. Warrick, A. N. Pfeiffer, M. J. Bell, D. J. Haxton, C. W. McCurdy, D. M. Neumark, and S. R. Leone, J. Phys. B **87**, 013415 (2015).
[66] S. Chen, M. Wu, M. B. Gaarde, and K. J. Schafer, Phys. Rev. A **88**, 033409 (2013).
[67] M. Eckstein, C.-H. Yang, F. Frassetto, L. Poletto, G. Sansone, M. J. J. Vrakking, and O. Kornilov, Phys. Rev. Lett. **116**, 163003 (2016).
[68] D. J. Haxton, K. V. Lawler, and C. W. McCurdy, Phys. Rev. A **83**, 063416 (2011).